

# DISK WIND FEEDBACK FROM HIGH-MASS PROTOSTARS

JAN E. STAFF

College of Science and Math, University of the Virgin Islands, St Thomas, 00802, United States Virgin Islands

KEI E. I. TANAKA

Department of Earth and Space Science, Osaka University, Toyonaka, Osaka 560-0043, Japan  
 and

Chile Observatory, National Astronomical Observatory of Japan, Mitaka, Tokyo 181-8588, Japan

JONATHAN C. TAN

Department of Space, Earth & Environment, Chalmers University of Technology, Gothenburg, Sweden  
 and

Department of Astronomy, University of Virginia, Charlottesville, Virginia, USA

(Dated:)  
*Draft version April 7, 2022*

## ABSTRACT

We perform a sequence of 3D magnetohydrodynamic (MHD) simulations of the outflow-core interaction for a massive protostar forming via collapse of an initial cloud core of  $60 M_{\odot}$ . This allows us to characterize the properties of disk wind driven outflows from massive protostars, which can allow testing of different massive star formation theories. It also enables us to assess quantitatively the impact of outflow feedback on protostellar core morphology and overall star formation efficiency. We find that the opening angle of the flow increases with increasing protostellar mass, in agreement with a simple semi-analytic model. Once the protostar reaches  $\sim 24 M_{\odot}$  the outflow's opening angle is so wide that it has blown away most of the envelope, thereby nearly ending its own accretion. We thus find an overall star formation efficiency of  $\sim 50\%$ , similar to that expected from low-mass protostellar cores. Our simulation results therefore indicate that the MHD disk wind outflow is the dominant feedback mechanism for helping to shape the stellar initial mass function from a given prestellar core mass function.

## 1. INTRODUCTION

Bipolar jets and outflows are commonly observed from accretion disks around low-mass protostars (e.g., Bacciotti et al. 2000; Ray et al. 2007; Coffey et al. 2008). The launching of this outflow is thought to be due to magnetocentrifugal acceleration (Blandford & Payne 1982; Konigl & Pudritz 2000), in which a large-scale magnetic field threads the accretion disk. Gas can flow along the magnetic field lines if they are inclined sufficiently with respect to the disk. The gas gains speed as it flows along the field lines. Beyond the Alfvén surface, the field lines will become twisted, which collimates the flow. Although typically more difficult to observe, high-mass protostars are also often seen to have associated jets and outflow (e.g., Arce et al. 2007; Beltrán & de Wit 2016; Hirota et al. 2017). Indeed, outflows are very commonly seen in most astrophysical settings where there is an accretion disk surrounding a central object, and the magnetocentrifugal model was first proposed for AGN jets. The disk wind mechanism has been studied extensively with numerical simulations (e.g., Shibata & Uchida 1985; Uchida & Shibata 1985; Ouyed & Pudritz 1997; Romanova et al. 1997; Ouyed et al. 1997, 2003; Ramsey & Clarke 2011; Anderson et al. 2006; Moll 2009; Staff et al. 2010, 2015; Stute et al. 2014). Other models for launching the outflow have also been proposed. For instance, an outflow may originate in the innermost part of the disk or the disk/magnetosphere boundary (often referred to as the X-wind model, Lovelace et al. 1991; Shu et al. 2000), a

stellar wind (Matt & Pudritz 2005), or driven by the magnetic pressure of the magnetic field (i.e., magnetic tower model of Lynden-Bell 1996).

One possible formation scenario for high-mass stars is that of Core Accretion, i.e., it is simply a scaled-up version of the standard model for low-mass star formation by accretion from gravitationally bound cores (Shu, Adams & Lizano 1987). In the Turbulent Core Model (McKee & Tan 2002, 2003), a combination of turbulence and magnetic pressure provide most of the support in a massive core against gravity. In high pressure conditions typical of observed massive star forming regions, the accretion rate from such massive cores is expected to be relatively high, i.e., with  $\sim 10^{-4}$  to  $\sim 10^{-3} M_{\odot} \text{ yr}^{-1}$ , compared to lower-mass protostars in lower pressure regions, i.e., with  $\sim 10^{-6}$  to  $\sim 10^{-5} M_{\odot} \text{ yr}^{-1}$ . In this scenario, the outflows from forming massive stars may therefore also be a scaled-up version of the outflows from lower-mass stars, but with much higher mass outflow rates and momentum rates. Alternative formation scenarios include models in which multiple smaller objects form close together, and then collide to form larger stars (Bonnell et al. 1998), and Competitive Accretion (Bonnell et al. 2001), in which stars forming in central, dense regions of protoclusters accrete most of their mass from a globally collapsing reservoir of ambient clump material (see Tan et al. 2014 for a review). In these models, outflows are expected to be more disordered.

There are some observations of highly collimated jets

from massive young stellar objects (YSOs). For example, Marti et al. (1993) found a bipolar jet from the central source between HH 80 and 81. McLeod et al. (2018) reported observations of HH 1177, a jet originating from a massive YSO in the Large Magellanic Cloud. Caratti o Garatti et al. (2015) observed jets from 18 intermediate and high mass YSOs, and found that these jets appear as a scaled-up version of jets from lower-mass YSOs. Carrasco-González et al. (2010) and Sanna et al. (2015) studied the magnetic field morphology near massive YSOs, and found a magnetic field configuration parallel to the outflow and perpendicular to the disk. Observations of wider angle, but still collimated, molecular outflows have also been reported: see for instance Beuther et al. (2002); Maud et al. (2015); Wu et al. (2004); Zhang et al. (2014a, 2013b). The general trend found in these works is that a more luminous (and hence generally more massive) protostar has more massive and powerful outflows, perhaps with larger opening angles.

The collapsing gas in a core may be dispersed by the outflows and jets coming from forming stars (e.g., Matzner & McKee 2000). This occurs both because some gas is ejected from the accretion disk into the outflow, and also because the outflow sweeps up gas in the core as it propagates outwards. This feedback on the core can therefore regulate star formation. The core to star formation efficiency (SFE) is denoted by  $\epsilon_{\text{core}}$  and defined to be the final mass of the star divided by the initial core mass. Understanding the SFE can allow for the transformation of the (prestellar) core mass function (CMF) to the stellar initial mass function (IMF).

Zhang et al. (2014b) performed semi-analytic modeling and radiative transfer calculations of massive protostars forming from massive cores, based on the turbulent core model and including disk wind outflow feedback. They found that a  $60 M_{\odot}$  core resulted in a  $26 M_{\odot}$  star, i.e., a SFE of  $\sim 43\%$ . Kuiper et al. (2016) performed axisymmetric radiation hydrodynamic (HD) simulations with the subgrid module for protostellar outflow feedback of  $100 M_{\odot}$  cores, and found SFEs of  $\sim 20\% - 50\%$ . Using semi-analytic models extended from those of Zhang et al. (2014b), Tanaka et al. (2017) studied feedback during massive star formation, and found the disk wind to be the dominant feedback mechanism, with overall SFEs of  $\sim 30 - 50\%$ . Machida & Matsumoto (2012) investigated the SFE in low mass cores by doing resistive magnetohydrodynamic (MHD) simulations, and found a SFE of  $\lesssim 50\%$  in those cases. Matsushita et al. (2017) and Matsushita et al. (2018) presented results of MHD simulations of outflows from massive YSOs. Their results indicated that massive stars can form through the same mechanism as low mass stars, though they did not follow the evolution until the end, and therefore could not estimate the SFE.

Observationally, Könyves et al. (2010) and André et al. (2010) reported that in relatively low mass clusters, the CMF and IMF have similar shapes, but the CMF is shifted to higher masses by a factor a few. Cheng et al. (2018) have measured the CMF in a more massive protocluster finding a similar shape as the Salpeter IMF, which may indicate that SFE is relatively constant with core mass. However, Liu et al. (2018) and Motte et al. (2018) have claimed shallower, i.e., top-heavy, high-end CMFs, which may imply SFEs become smaller at higher

masses, potentially consistent with the results of Tanaka et al. (2017).

Here we present results of three dimensional ideal MHD simulations of the outflow from a protostar, forming from an initial core of  $60 M_{\odot}$ . With these MHD simulations, we aim to test the semi-analytic modeling of Zhang et al. (2014b). We describe the method in §2. We present our results in §3, and discuss them in §4 where we also summarize our results.

## 2. METHODS

In this work we study the impact of MHD outflows in massive star formation under the framework of the Turbulent Core Model (McKee & Tan 2003), which is a scaled-up version of low-mass star formation. In this section we introduce our model: a schematic view is shown in Figure 1.

### 2.1. Overview

We consider the formation of a single massive star from the collapse of a cloud core with initial mass of  $M_c = 60 M_{\odot}$ . The core is assumed to be in pressure equilibrium with the ambient clump. With a typical mass surface density for high-mass star-forming clumps of  $1 \text{ g cm}^{-2}$ , the core radius  $R_c$  is  $0.057 \text{ pc}$  or  $\simeq 12,000 \text{ au}$  (McKee & Tan 2003). The infalling material accretes onto the central protostar from a disk. The accretion process drives a disk wind via the magnetocentrifugal mechanism (Blandford & Payne 1982), creating a large outflow that reduces the infall rate and the SFE from the core. To investigate the properties of the MHD-driven outflow and the SFE, we perform 3-D MHD simulations using ZEUS-MP (Norman 2000). Similar to the goals of our study, Zhang et al. (2014b) performed a semi-analytic calculation based on the Turbulent Core Model with the disk-wind feedback model of Matzner & McKee (2000). They found the final stellar mass to be  $\sim 26 M_{\odot}$  from a  $60 M_{\odot}$  core, i.e., the SFE was  $\sim 43\%$ .

We use Cartesian coordinates  $(x_1, x_2, x_3)$  to describe our domain, which contains most of one hemisphere, i.e.,  $100 \text{ au} < x_1 < R_c + \zeta_x$ ,  $-R_c - \zeta < x_2 < R_c + \zeta$ , and  $-R_c - \zeta < x_3 < R_c + \zeta$ , with  $\zeta_x$  and  $\zeta$  ensuring that the boundary is outside of the core. The exact values of  $\zeta_x$  and  $\zeta$  depend on the simulation. In order to be able to cover the entire core-scale on the grid, while maintaining a reasonable resolution near the axis, we use a Cartesian coordinate system with logarithmically spaced grid cells (“ratioed” grid in ZEUS terminology). This means that in the  $x_1$  direction, the grid cells are fairly small (please see below for details) near the inner  $x_1$  boundary, and gradually become larger farther away from this boundary. In the  $x_2$  and  $x_3$  directions, the grid cells are fairly small near the central axis, and gradually become larger farther away from the axis. As a consequence, the grid cells can become rather large and deviate substantially from a cubic shape in the outer regions of the core. To ensure that these rather coarse grid cells do not affect the dynamics, we have also performed two comparison simulations with higher resolution (see §3.5).

Note that the inner  $x_1$  boundary is at  $100 \text{ au}$  above the star-disk system. Hence the accretion onto the star-disk system and the launching of the disk wind are not explicitly solved in this work. Instead, a flow is injected from a circular region on the inner  $x_1$  boundary, which

imitates the disk wind. We will describe this flow in more detail in §2.2.

The number of grid cells varies between the simulations, with the 1 and 2  $M_\odot$  simulations having more cells as the injection region is relatively smaller compared to the core size than in the higher mass simulations. We aim at resolving the scale of the disk wind injection region,  $r_{\text{inj}}$ , with  $\sim 10$  cells across. Since the injection region depends on the disk size, which depends on the protostellar mass, this dictates how small the smallest cells around the axis can be. There is a limit to how large a ratio between one cell and the next ZEUS-MP will allow, which therefore sets a lower limit on how many grid cells are needed in order to cover the whole core-hemisphere. This leads us to use a grid with  $140 \times 260 \times 260$  cells in our standard setup for these simulations (with  $m_* \geq 4 M_\odot$ ), and  $210 \times 380 \times 380$  cells for the  $m_* = 1$  and 2  $M_\odot$  simulations. To test the effect of grid resolution on the results, we also ran the 4  $M_\odot$  simulation using a grid with  $210 \times 380 \times 380$  cells (medium resolution), and using a grid with  $280 \times 520 \times 520$  cells (i.e., double the number of cells; high resolution).

The inner  $x_1$  boundary is a special boundary, where the density and velocity are held constant at all times, while the magnetic field is allowed to evolve. Keeping the magnetic field fixed on the  $x_1$  boundary, as was done in Staff et al. (2015), caused numerical problems in some of our simulations, since the collapsing core in these cases significantly altered the magnetic field just above this boundary. All other boundaries are normal ZEUS outflow boundaries.

Our outflow simulations consist of a sequence of models with  $m_* = 1, 2, 4, 8, 16$ , and 24  $M_\odot$ . The idea is that each stage is run for a relatively short time that is less than the overall expected formation time of the star, to examine the quasi equilibrium behavior of the system, especially the opening angle ( $\theta_{\text{outflow}}$ ) of the outflow cavity. At each stage, the protostellar disk is expected to be massive and possibly moderately self-gravitating due to the high mass supply from the infalling envelope. The angular momentum would then be transported efficiently by torques in the disk keeping the mass ratio of disk and star roughly constant at  $f_d = 1/3$ . With this assumption, we then set the envelope mass as  $M_{\text{env}} = M_c - (1 + f_d)m_*$  for the initial condition for each simulation. This means that the material ejected by the outflow earlier in the evolution is ignored, but this earlier ejection will be approximated by early evolution of each simulation as it approaches quasi-equilibrium. To test this approximation, once the opening angle is seen to become significant, we also run a sequence of models with  $m_* = 4, 8, 16$ , and 24  $M_\odot$  where the initial setup has a “pre-cleared” cavity mimicking the effect of the outflow earlier in the evolution.

While the density structure of the fiducial prestellar core in the Turbulent Core Model is assumed to be spherical with a power law of the form  $\rho \propto r^{-1.5}$  (see McKee & Tan 2003), as the collapse starts, the density profile is expected to become shallower. Thus, based on the self-similar solution of the inside-out collapse (Shu 1977; McLaughlin & Pudritz 1997), we assume an index of  $-1$  as the initial condition for the density profile of the in-

falling envelope:

$$\rho_{\text{env}}(t=0) = \rho_{\text{env,out}} (r/R_c)^{-1}, \quad (1)$$

where  $r$  is the distance from the stellar center, and  $\rho_{\text{env,out}}$  is a normalization density to give the appropriate total mass of the envelope, i.e.,  $M_{\text{env}} = M_c - (1 + f_d)m_*$ . Although the collapse has started, we assume initial velocities in the envelope to be zero for simplicity. We approximate the gas as being isothermal, with a temperature of 100 K, giving a sound speed  $c_s = 0.6 \text{ km s}^{-1}$  for molecular gas.

We include the gravitational potential from the protostar, which is taken to be a point mass of  $m_*$ . For the infall envelope, for simplicity we also treat this via a static gravitational potential based on the initial gas mass distribution in the core, i.e., mass  $M_{\text{env}}$ . Note that in this approximation the minor contribution to the potential of the disk is ignored. Tests show that this only has minor effects on the results.

The core is threaded by a magnetic field, which has two contributions. There is a “Blandford-Payne” like force-free disk-field originating on the accretion disk (the poloidal magnetic field on the midplane is given by  $r^{-1.25}$ , Blandford & Payne 1982; Jørgensen et al. 2001). This disk field is normalized as in Staff et al. (2015) (assuming equipartition at the inner edge of the disk; which we assume extends all the way to the stellar surface), scaled to the relevant protostellar mass in each simulation. In addition, we add a constant field in the  $x_1$  direction to this field everywhere, so that the total flux of the initial core is  $1 \text{ mG} \times R_c^2$ . The constant field dominates over the disk field in the outer regions of the core.

We also run the  $m_* = 16 M_\odot$  simulation with no magnetic field as a test case. Here, we keep the setup from the regular runs, and simply set the magnetic field strength everywhere to zero. The outflow material is therefore injected in the same direction as in the simulation with magnetic field. This simulation helps to illustrate the role played by the magnetic field.

We run each simulation for an amount of time needed for the star to accrete half of the mass needed to bring it to the next simulated model based on the analytic accretion rates of the Turbulent Core Model. That is, we run the 8  $M_\odot$  simulation until it would have accreted 4  $M_\odot$  if no mass was ejected, which is roughly 15,000 years for the 8  $M_\odot$  simulation. The 24  $M_\odot$  was run for  $\sim 12,000$  years until it would have accreted  $\sim 4 M_\odot$ .

## 2.2. Injection of the disk wind

One of our objectives is to test the semi-analytic modeling of Zhang et al. (2014b), and we therefore ensure that the mass flow and momentum rates are similar to those in that work. Our injection boundary is at a height of  $\sim 100 \text{ au}$  above the disk, and to find the density profile of the flow there, we used the results of the simulations in Staff et al. (2015), which lead to a  $-1$  power law. We also obtain the velocity profile at a height of  $\sim 100 \text{ au}$  from the Staff et al. (2015) work.

As described above, the outflow is injected from a circular region at the inner  $x_1$  boundary at a height above the star-disk system of  $z_{\text{inj}} = 100 \text{ au}$  (see Figure 1). The injection velocity along the  $x_1$  direction is given by:

$$v_{\text{inj}} = (R_{\text{cyl}}/r_*)^{-1/2} \phi_m v_{\text{K}*}, \quad (2)$$

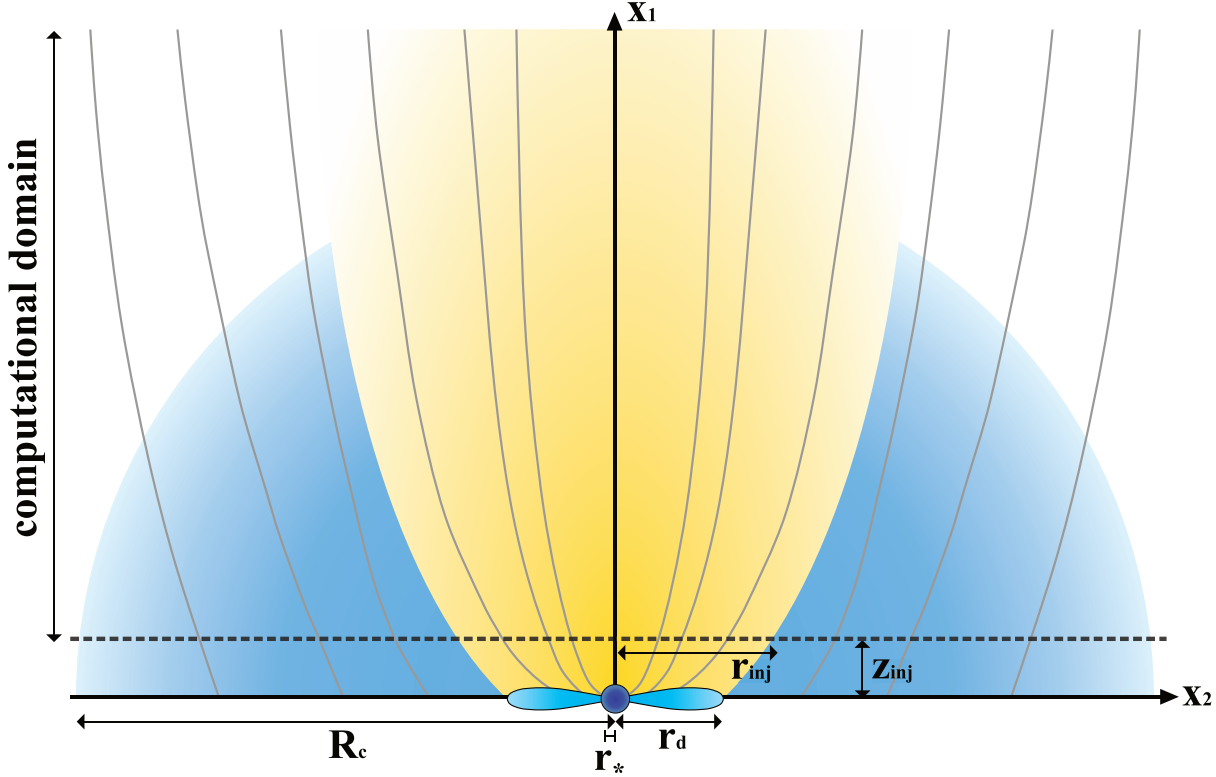


**Figure 1.** Schematic illustration of the setup. The  $x_3$  direction is perpendicular to this, and similar to  $x_2$ . The zero-point on the  $x_1$  axis is on the protostar. Also shown is the disk, the injection region, outflow, and core infall envelope. The gray lines illustrate the shape of the initial magnetic field lines.

where  $v_{K*}$  is the Keplerian velocity at the stellar surface,  $\phi_m$  is a dimensionless factor between 40 and 100 to ensure that the injected mass and momentum rates are equal to those of Zhang et al. (2014b), and  $R_{\text{cyl}} = \sqrt{x_2^2 + x_3^2}$  is the distance from the axis. Note that  $v_{\text{inj}}$  described in the above equation is only the component directed in the  $x_1$  direction. However, the injected velocity is given additional components in the  $x_2$  and  $x_3$  directions to angle it in the same direction as the initial magnetic field. In addition, the injected flow is also given a toroidal velocity:

$$v_{\phi, \text{inj}} = 0.23 \left( \frac{R_{\text{cyl}}}{22.4 r_*} \right)^{-1/2} v_{K*}. \quad (3)$$

The injected speed and direction is kept constant throughout the simulation. The toroidal (rotational) speed is only a few percent of the poloidal speed, so this only leads to a small deviation from the initial field direction. As the magnetic field evolves throughout the simulation, the deviation may however change at later times.

The density of the injected disk wind material is given by

$$\rho_{\text{inj}} = \begin{cases} \exp(0.0289 R_{\text{cyl}}/r_*) \phi_\rho \rho_0 & R_{\text{cyl}} < x_0 \\ 2.77 \left( \frac{R_{\text{cyl}}}{x_0} \right)^{-1} \phi_\rho \rho_0 & R_{\text{cyl}} \geq x_0 \end{cases} \quad (4)$$

with  $x_0 = 35.3 r_*$  and  $\rho_0$  being the injection density on the axis, which is set to match the accretion rate and in the work of Zhang et al. (2014b) and by assuming that the injected mass flux is 10% of the accreted mass flux.

Such a fiducial ratio of mass outflow rate to accretion rate is consistent with observational estimates (e.g., Beuther et al. 2002; Beltrán & de Wit 2016), although these are quite uncertain. We note that in our simulations the resolution is larger than  $x_0$ , so we only use the second line in the above equation. The smallest cell size is in the highest resolution  $4 M_\odot$  simulation, where the smallest cells are  $50 r_*$ .

The injected density profile assumed in Zhang et al. (2014b) is  $\rho_{\text{inj}} \propto x^{-1.5}$  at the disk. At a height of 100 au in that work, the density profile follows a power of  $-1.25$  for the innermost 15 au, but deviates substantially at larger radii. It is because of this difference, and because we have limited resolution in our simulations, that we need the factor  $\phi_\rho$  in the expression for  $\rho_{\text{inj}}$ , and  $\phi_m$  in the expression for  $v_{\text{inj}}$  in order to obtain the same mass flow and momentum rate as in Zhang et al. (2014b).

The setup parameters for the simulations are summarized in Table 1. The width of the flow at a height of 100 au has been calculated based on the shape of the field lines in the “Blandford-Payne” magnetic field configuration (eq. B22 in Zhang et al. 2013a):

$$\frac{r_{\text{inj}}}{r_d} = 1 + 14 \ln \left( 1 + 0.07 \frac{z_{\text{inj}}}{r_d} \right), \quad (5)$$

where  $r_d$  is the disk radius. The stellar and disk radii for the various protostellar masses are taken from Zhang et al. (2014b).

### 2.3. Calculating $\theta_{\text{outflow}}$

We are particularly interested in the opening angle ( $\theta_{\text{outflow}}$ ) of the outflow, since this is a quantity that is

**Table 1**

Summary of the setup parameters for the simulations.  $m_*$  is the mass of the protostar,  $r_*$  is the radius of the protostar,  $r_d$  is the radius of the disk,  $r_{\text{inj}}$  is the radius of the injection region,  $v_{K*}$  is the Keplerian speed at the protostellar surface,  $\rho_0$  is the injection density on the axis,  $\rho_{\text{env,out}}$  is the density at the core boundary,  $B_*$  is the disk magnetic field at the surface of the protostar,  $\dot{m}_{\text{inj}}$  is the rate of mass injection (into one hemisphere), and  $\dot{p}_{\text{inj}}$  is the rate of momentum injection (into one hemisphere).

| $m_*$<br>[ $M_\odot$ ] | $r_*$<br>[ $R_\odot$ ] | $r_d$<br>[au] | $r_{\text{inj}}$<br>[au] | $v_{K*}$<br>[km s $^{-1}$ ] | $\rho_0$<br>[cm $^{-3}$ ] | $\rho_{\text{env,out}}$<br>[cm $^{-3}$ ] | $B_*$<br>[G] | $\dot{m}_{\text{inj}}$<br>[ $M_\odot$ yr $^{-1}$ ] | $\dot{p}_{\text{inj}}$<br>[ $M_\odot$ yr $^{-1}$ km s $^{-1}$ ] |
|------------------------|------------------------|---------------|--------------------------|-----------------------------|---------------------------|--|--------------|--|---|
| 1                      | 2.61                   | 13.1          | 91.9                     | 270.31                      | $2.9 \times 10^8$         | $1.6 \times 10^6$                        | 324.35       | $5.0 \times 10^{-6}$                               | 0.0025  |
| 2                      | 3.45                   | 20.9          | 105.7                    | 332.50                      | $1.7 \times 10^8$         | $1.6 \times 10^6$                        | 305.58       | $7.1 \times 10^{-6}$                               | 0.0050  |
| 4                      | 20.5                   | 34.2          | 123.7                    | 192.90                      | $2.3 \times 10^7$         | $1.5 \times 10^6$                        | 68.152       | $1.0 \times 10^{-5}$                               | 0.0047  |
| 8                      | 33.4                   | 57.1          | 150.0                    | 213.73                      | $1.1 \times 10^7$         | $1.3 \times 10^6$                        | 51.105       | $1.3 \times 10^{-5}$                               | 0.0071  |
| 16                     | 6.41                   | 101.0         | 196.4                    | 689.95                      | $3.3 \times 10^7$         | $1.0 \times 10^6$                        | 271.99       | $1.6 \times 10^{-5}$                               | 0.021   |
| 24                     | 6.38                   | 185.0         | 282.0                    | 848.6                       | $2.0 \times 10^7$         | $7.4 \times 10^5$                        | 262.83       | $1.7 \times 10^{-5}$                               | 0.025   |

directly related to the star formation efficiency and is a measurable quantity in real protostellar cores. It was also calculated by Zhang et al. (2014b), and can therefore be compared with their work. After some experimentation, we have automated the calculation of  $\theta_{\text{outflow}}$ . To calculate it, we search through the grid for forward velocities  $v_1 > c_s = 0.6$  km s $^{-1}$ . Starting from the outside grid boundary, we seek through the grid along the principal axes towards the axis, and take the first instance of such velocity to be the edge of the flow. We then draw a straight line from there to the protostar (the center of the core). The angle that this line makes with the normal to the disk we call  $\theta_{\text{outflow}}$ . As the flow is not entirely symmetric, we do this along both the  $x_2$  and the  $x_3$  directions, from both boundaries, and take  $\theta_{\text{outflow}}$  of the flow to be the average of these.

#### 2.4. Pre-cleared cavity

As described above, our first set of simulations ignore the earlier evolutionary stages in the development of the outflow cavity. To explore the potential effects of this approximation, we run another sequence of models with  $m_* = 4, 8, 16$ , and  $24 M_\odot$ , with each model having a cavity pre-cleared based on the results of the lower mass model without pre-clearing. That is, the pre-cleared cavity in the  $4 M_\odot$  simulation was made to be similar to the outflow cavity in the  $2 M_\odot$  simulation (without pre-clearing) when that protostar would have accreted half the mass needed to make it the next model that we simulate. The pre-cleared cavity in the  $8 M_\odot$  simulation was made similar to the outflow cavity in the  $4 M_\odot$  simulation without pre-clearing, etc. In the pre-cleared region, we simply reduced the density by a factor of ten compared to the simulation without pre-clearing. The pre-cleared region was defined to be:

$$R_{\text{cyl}} = R \sin \theta_{\text{clearing}} + 50 \left( \frac{R_\odot}{r_*} \right) \text{ au} \quad (6)$$

where  $R_{\text{cyl}} = \sqrt{x_2^2 + x_3^2}$  is the cylindrical distance from the axis ( $x_2 = 0$  and  $x_3 = 0$ ),  $R$  is the distance from the protostar, and  $\theta_{\text{clearing}}$  is the opening angle  $\theta_{\text{outflow}}$  of the previous lower-mass simulation (Table 2). This expression was found to mimic the cavity found in the simulations without pre-clearing reasonably well.

### 3. RESULTS

#### 3.1. General outflow morphologies and velocity distributions

We perform a sequence of disk wind protostellar outflow simulations with the protostellar mass increasing from 1 to  $24 M_\odot$  and the initial envelope mass declining from  $\sim 59 M_\odot$  to  $\sim 28 M_\odot$ , which maintains the constant total of  $60 M_\odot$  (of the envelope, the protostar, and the disk; see above). In Figure 2 we show a slice of the H nuclei number density,  $n_{\text{H}}$  (i.e., number density of H nuclei in units of cm $^{-3}$ , where we have assumed a mass per H nucleus of 1.4 proton masses to account for He), through the middle of the grid at the end of the simulations, for the cases with protostellar masses of 1, 2, 4, 8, 16, and  $24 M_\odot$ . Figure 3 shows the same, but only showing the material with a positive  $v_1$  velocity component (i.e., outflowing material). Overlayed on that is yellow line showing the opening angle as found in Zhang et al. (2014b), and a blue line showing the opening angle that we find in this work. In all simulations, the outflow carves out a low density cavity. However, higher density gas outside of this cavity is also outflowing, and  $\theta_{\text{outflow}}$  is therefore larger than just the size of the cavity. As described in §2, the time of the snapshots shown in Figure 2 is after an amount of time needed for the star to accrete half of the mass needed to bring it to the next simulated model.

In Figure 4 we show histograms of the distribution of the outflowing mass from one hemisphere with respect to the outflow velocity ( $v_1$ ), first at an early stage of the simulations near the point of first break out from the core, and then at the end of the simulations. In the latter, the lower mass simulations show a peak around 10 km s $^{-1}$ , while the higher mass simulations show a peak around 30 km s $^{-1}$ . Figure 4 also shows a comparison of the simulated distributions of outflow mass with speed with two observed protostars, C1-Sa and C1-Sb, studied by Tan et al. (2016). The shape of the distributions of C1-Sa's blueshifted outflow and C1-Sb's redshifted outflow are quite similar to some of the simulations, especially those at later times, when the lower velocity flow has had more time to become established. However, C1-Sa's redshifted outflow and C1-Sb's blueshifted outflow show significantly larger amounts of mass at higher velocities (and note that these distributions are not corrected for inclination, so are actually even higher). We note, however, that the outflow properties from these sources were measured on scales extending 12'' from the protostar, or 60,000 au. This is much larger than our simulation box of  $\sim 12,000$  au. In our simulations, much material, and in particular high velocity material, has left the simulation box (see Table 2).

**Table 2**

The final opening angle ( $\theta_{\text{outflow}}$ ) found in the simulations for the various protostellar masses, after a time when the star would have accreted half the mass needed to take it to the next simulated protostellar mass (the 24  $M_{\odot}$  simulation has accreted 4  $M_{\odot}$ ). Also listed is the total mass that has flown out of one hemisphere during each simulation.

| Mass of star<br>[ $M_{\odot}$ ] | $\theta_{\text{outflow}}$<br>pre-clearing<br>[degrees] | $\theta_{\text{outflow}}$<br>no pre-clearing<br>[degrees] | Total mass outflow<br>pre-clearing<br>[ $M_{\odot}$ ] | Total mass outflow<br>no pre-clearing<br>[ $M_{\odot}$ ] |
|---------------------------------|--|---|---|--|
| 1                               | -  | 8.4   | -   | 0.35   |
| 2                               | -  | 15.0  | -   | 0.88   |
| 4                               | 15.7   | 14.9  | 0.28  | 0.70   |
| 8                               | 25.1   | 28.8  | 1.06  | 1.60   |
| 16                              | 49.0   | 42.0  | 2.05  | 2.75   |
| 24                              | 77.0   | 62.0  | 2.38  | 3.34   |

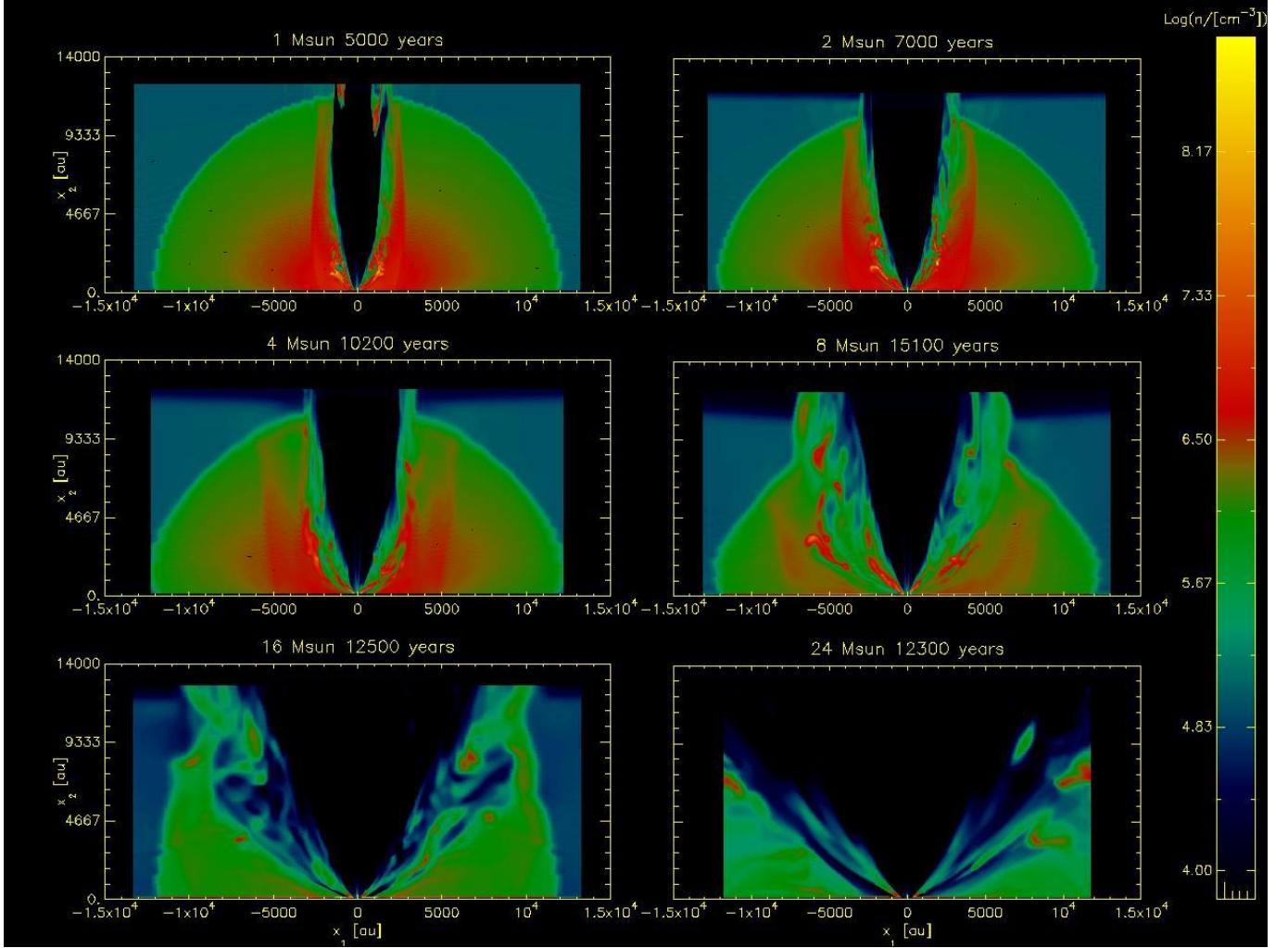


**Figure 2.** Slices through the middle of the simulation domains (in the  $x_1 - x_2$  plane) showing density structures ( $n_{\text{H}}$ ) of the massive protostellar cores for fiducial runs with protostellar masses of 1, 2, 4, 8, 16, and 24  $M_{\odot}$ , as labelled. Outputs are shown after various amounts of time evolution (see text).

In Figure 5 we show the distribution of the outflowing mass with respect to the outflow density, at the end of each simulation. Most outflowing mass in the 24  $M_{\odot}$  simulation is found to be around  $n_{\text{H}} \sim 10^5 - 10^6 \text{ cm}^{-3}$ . For the lower-mass simulations, the distribution is bimodal with most mass is at a slightly higher density of around  $2 \times 10^6 \text{ cm}^{-3}$  and another peak at  $\sim 10^5 \text{ cm}^{-3}$ . The 16  $M_{\odot}$  simulation is in between, with a much broader

peak stretching from  $\sim 5 \times 10^4$  to  $\sim 10^6 \text{ cm}^{-3}$ .

In Figure 6 we show the logarithm of the magnetic field strength in a slice through the middle of the grid at the end of each simulation. It is evident that the magnetic field strength within the outer outflow cavity is relatively weak, with  $B \ll 1 \text{ mG}$ , i.e., much lower than the background core's ambient  $B$ -field. However, the  $B$ -field strengths at the base of the outflow are much stronger, i.e., with values approaching  $\sim 100 \text{ mG}$  in the



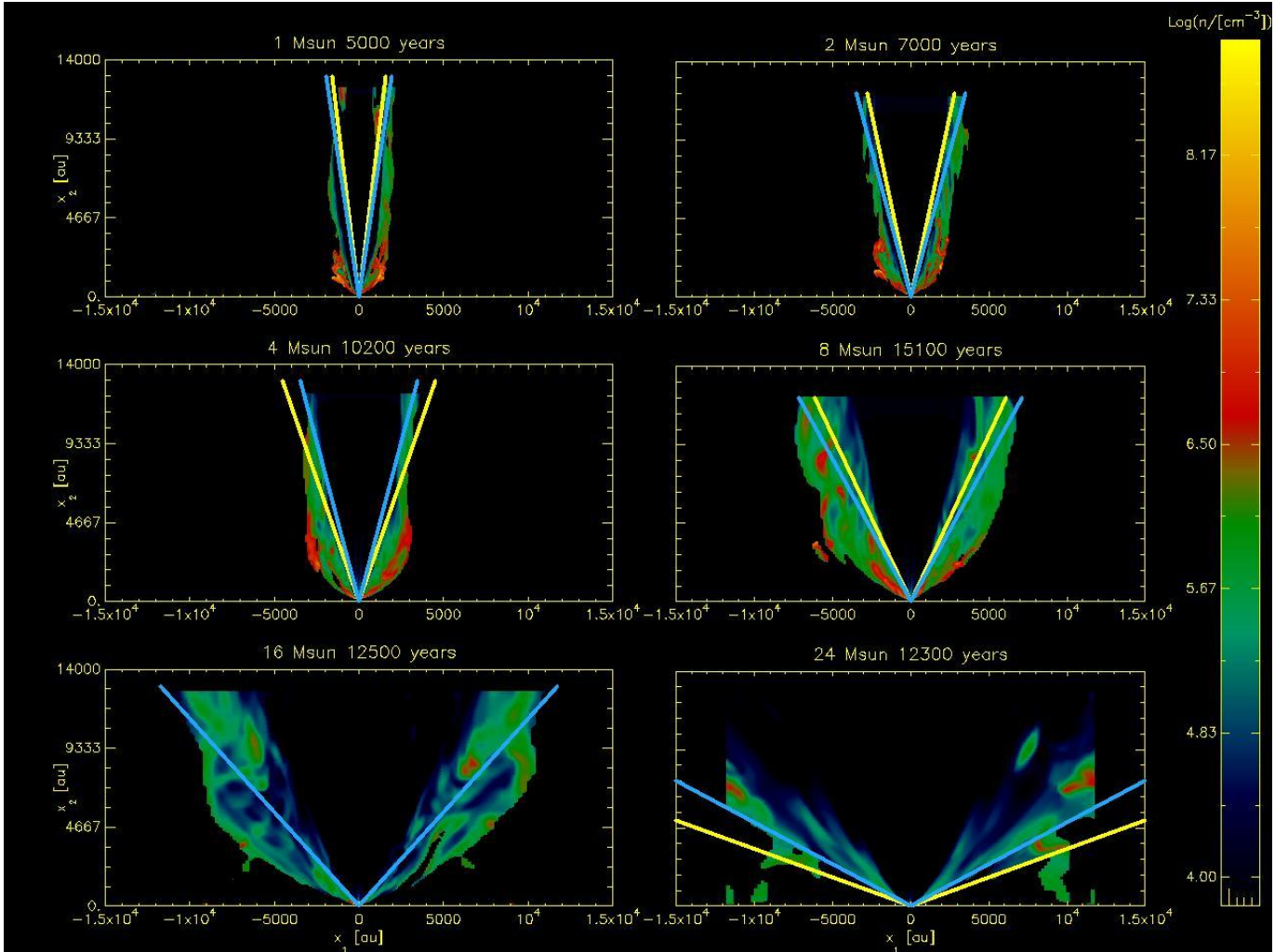


**Figure 3.** The same as Fig. 2, but only showing the density that has a positive velocity in the  $x_1$  direction. This therefore shows the structure of the outflow. The yellow “V”-shaped lines show  $\theta_{\text{outflow}}$  found in the semi-analytic models of Zhang et al. (2014b), while the light blue “V”-shaped lines show the opening angle that we find in this work. Note that in the  $16 M_{\odot}$  simulation, the blue and yellow lines are on top of each other, as the opening angle that we found matches that from Zhang et al. (2014b).

highest mass cases.

### 3.2. Outflow opening angle

Figure 7 shows the time evolution of  $\theta_{\text{outflow}}$  in each of the fiducial simulations, i.e., without pre-clearing. In each individual simulation  $\theta_{\text{outflow}}$  grows from zero from the time when the outflow has just managed to break out of the initial core envelope structure, typically after  $\lesssim 1,000$  years, depending on  $m_*$ . In the case of the 1, 2, 4 and  $8 M_{\odot}$  runs,  $\theta_{\text{outflow}}$  then increases fairly steadily. For the  $16 M_{\odot}$  case, there is more rapid initial expansion as the outflow cavity is established, and then a more distinct phase of gradual widening. Finally for the  $24 M_{\odot}$  case, the expansion is fast and quite steady for the full duration of the simulated period, with only a modest decrease in the rate of expansion during the later evolution.

As described above, a natural time to consider the outputs of the simulation is after the protostar has had sufficient time to increase its mass significantly, i.e., half-way towards the next model in the sequence<sup>1</sup>. These times are

<sup>1</sup> Note in the case of the  $24 M_{\odot}$  protostar we list the result at a time of 12,000 yr, i.e., after it has had time to accreted  $4 M_{\odot}$ .

used to evaluate the “final”  $\theta_{\text{outflow}}$  that is listed in Table 2. In Figure 7, these times are marked by vertical dotted lines. Also shown in this figure are  $\theta_{\text{outflow}}$  expected in the semi-analytic models of Zhang et al. (2014b). At our adopted output times, these semi-analytic estimates compare very well with those of our MHD simulations: they are generally within about 5 degrees of each other.

At a given time, including our chosen “final” output times,  $\theta_{\text{outflow}}$  is generally larger for models with more massive protostars. This can also be seen in Figure 8, which shows  $\theta_{\text{outflow}}$  versus protostellar mass. The main exception is the  $4 M_{\odot}$  case, which has a slightly smaller  $\theta_{\text{outflow}}$  compared to the  $2 M_{\odot}$  case. The reason for this is that at  $4 M_{\odot}$  the protostar has evolved into a relatively large, expanded size. This means the Keplerian speed at the disk inner edge is relatively low so that the disk wind outflow is relatively weak. For this case, the effects of pre-clearing, discussed below, are expected to be more important. Figure 8 compares our simulation results to the semi-analytic model estimates of Zhang et al. (2014b). It is apparent that the numerical results agree well with the semi-analytic model predictions.

In addition to the simulations described above, we per-

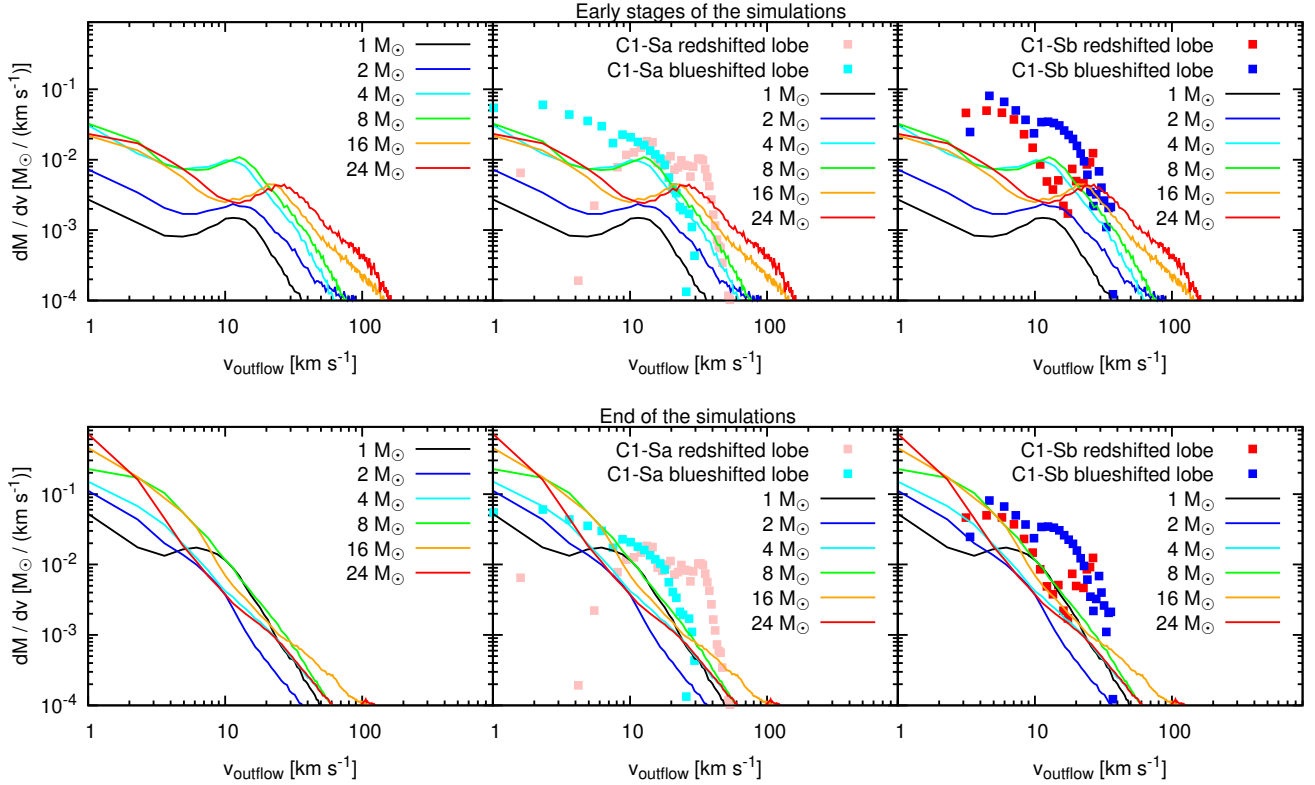


**Figure 4.** *Upper left panel:* Histogram showing the distribution of the outflow mass with respect to the outflow speed, evaluated around the time that the outflow breaks out of the core in each simulation. The bin width is  $1.3 \text{ km s}^{-1}$ . *Upper middle panel:* The same, but with the C1-Sa data shown also. *Upper right panel:* The same, but with the C1-Sb data shown also. The C1-Sa and C1-Sb data is from Tan et al. (2016). The bottom row shows the same, but at the end of the simulations, at which point much mass has left the computational domain.

formed a sequence of simulations where the initial setup has a pre-cleared cavity (starting with the  $4 M_{\odot}$  simulation) (see §2.4). We find that  $\theta_{\text{outflow}}$  (see Table 2 and Figure 8) is not much different whether or not we have pre-cleared a cavity, which indicates the general robustness of the results and the validity of ignoring prior evolution for each fiducial simulation run.

However,  $\theta_{\text{outflow}}$  in the  $24 M_{\odot}$  simulation with pre-clearing does open up faster and to a greater extent ( $\theta_{\text{outflow}} = 77.0^{\circ}$ ) than in the simulation without pre-clearing ( $\theta_{\text{outflow}} = 62.0^{\circ}$ ). Interestingly, in the  $8 M_{\odot}$  simulation,  $\theta_{\text{outflow}}$  is smaller with pre-clearing than without. This may be due to the outflow feedback being more easily directed into the low-density initial cavity, i.e., deflecting off the dense core infall envelope, and so more easily confined. In the case without the initial cavity, the outflow may be able to establish a broader opening angle during its initial break-out phase.

### 3.3. Mass flow rate and momentum rate

Figures 9 and 10 show the mass outflow and momentum rate measured at a height of  $R_c$  above the disk, as a function of time for our simulations. What we call mass outflow rate ( $\dot{m}$ ) is the mass flowing out of one hemisphere in the  $x_1$  direction only, and likewise what we call momentum rate ( $\dot{p}$ ) is only including the momentum in the  $x_1$  direction (from one hemisphere). Without pre-clearing, the flow rate for each simulation has a large “bump” in the early part of the simulation. This bump is a result of the initial state. In each sim-

ulation, the flow has to clear out a new outflow channel, leading to this artificial transient event. Once an outflow channel has been established by pushing the mass out of the simulation box, the flow rate stabilizes ( $\sim 10^{-4} M_{\odot} \text{ yr}^{-1}$  for the 4 and  $8 M_{\odot}$  simulations, and  $\sim 2 \times 10^{-4} M_{\odot} \text{ yr}^{-1}$  for the 16 and  $24 M_{\odot}$  simulations). The momentum rates also stabilizes after an initial transient phase ( $\sim 5 - 10 \times 10^{-3} M_{\odot} \text{ km s}^{-1} \text{ yr}^{-1}$  for the 4 and  $8 M_{\odot}$  simulations and  $\sim 2.5 \times 10^{-2} M_{\odot} \text{ km s}^{-1} \text{ yr}^{-1}$  for the 16 and  $24 M_{\odot}$  simulations). The effect of the pre-clearing is clearly seen in the mass outflow rate figure. With pre-clearing, there is still a “bump”, but it is much less prominent. The effect of the pre-clearing is also visible in the momentum rates, in that these are smoother at earlier times with pre-clearing than without. The mass flow and momentum rates stabilizes around the same values in the simulations with and without pre-clearing.

In Figure 11 we show the mass outflow rate at different heights above the disk in the envelope (at  $R_c$ ,  $R_c/2$ , and  $R_c/10$ ) as a function of the protostellar mass for both the simulations without and with pre-clearing. We find that the mass outflow rate at a height of  $R_c$  is generally higher for the larger protostellar masses ( $\sim 1 - 2 \times 10^{-4} M_{\odot} \text{ yr}^{-1}$  for the high-mass simulations compared to  $\sim 0.5 - 1 \times 10^{-4} M_{\odot} \text{ yr}^{-1}$  for the low-mass simulations) mainly due to the stronger injection (see Table 1). We also find that for the lowest mass simulations (1 and  $2 M_{\odot}$ ), the mass flow rate at  $R_c$  is larger than for the  $4 M_{\odot}$  simulation, in the case of no pre-clearing. In the high-mass simulations, the mass flow rate at  $1/10 R_c$



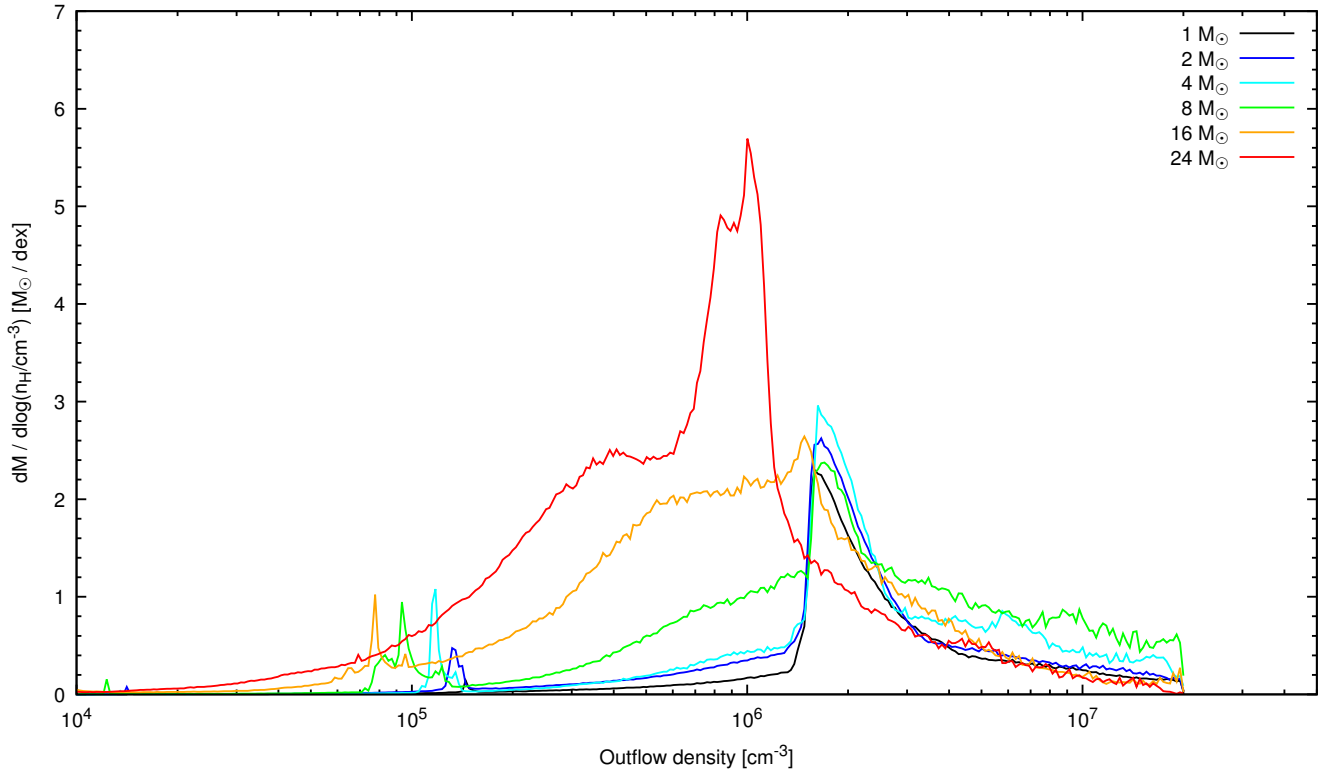


**Figure 5.** Distribution of the outflow mass with respect to the logarithm of H number density. The histogram is made from the last snapshot of each simulation. The bin width is 0.01 dex.

and  $1/2 R_c$  is a factor a few lower in the pre-cleared simulations than in the simulations without pre-clearing, which is attributed to more material being swept-up in the simulations without pre-clearing. The mass flow rate at  $R_c$  is generally larger than deeper in the core, due to more material being swept up. This mass flow rate at  $R_c$  is roughly 6 – 12 times the injected flow rate. Except for the lowest mass simulations, the mass flow rate at  $R_c$  is roughly the same in the simulations with and without pre-clearing.

Figure 12 shows the outflow momentum rate at different heights above the disk in the core as a function of protostellar mass. We find that the momentum rate is  $10^{-3} - 10^{-2} M_\odot \text{ km s}^{-1} \text{ yr}^{-1}$ , and that it grows slightly as the flow propagates through the core. The momentum rate exiting the core is slightly larger than the injected momentum rate. This slight increase in momentum rate is likely due to limited resolution, as it is not seen to the same extent in the high resolution simulation (see §3.5).

The total mass flowing out of one hemisphere (found by integrating the mass outflow rate over time) for each case is listed in Table 2. Summing all the simulations without pre-clearing, we find that  $9.62 M_\odot$  flowed out of one hemisphere in our simulations. With pre-clearing, the sum is  $5.77 M_\odot$ , though that excludes the 1 and  $2 M_\odot$  simulations. Since the simulations only run to half-way to accreting to the next stage, then the total mass expected to be ejected if continuous growth of the protostar were followed is expected to be about twice the above values, i.e.,  $2 \times \sim 6 M_\odot \simeq 12 M_\odot$  in the case with pre-clearing. Accounting for both hemispheres, the total outflowing mass becomes  $\sim 24 M_\odot$ , which is similar to

the mass growth of the protostar, demonstrating that the star formation efficiency is about 50% from the core during this evolution.

We show these stabilized (final) mass flow rates and momentum rates as a function of bolometric luminosity in Figure 13. The bolometric luminosity has been estimated based on the mass of the protostar following Zhang & Tan (2018). The figure also shows the best fit line for the momentum rate from the observational data in Wu et al. (2004), given by  $\log(\dot{P}/(M_\odot \text{ km s}^{-1} \text{ yr}^{-1})) = (-4.92 \pm 0.15) + (0.648 \pm 0.043) \log(L_{\text{bol}}/L_\odot)$  (we only plot the best fit line without uncertainty).

### 3.4. Comparing the effects of not rotating the injected flow and not having a B-field

We find that in the  $16 M_\odot$  simulation (without pre-clearing), after  $10^4$  years, there is very little difference whether the injected material is given rotation or not (see Figure 14). In both cases the opening angle at this particular time is  $\sim 42^\circ$ . In a test simulation without magnetic field we find that the opening angle is  $\sim 48^\circ$  at this particular time. However, we also find that the no magnetic field simulation has a larger outflowing mass rate than the simulation with magnetic field at this particular time. The simulation with magnetic field has a mass flow rate out of one hemisphere of  $2 \times 10^{-4} M_\odot \text{ yr}^{-1}$ , while the simulation without magnetic field has a mass flow rate of  $3 \times 10^{-4} M_\odot \text{ yr}^{-1}$  out of one hemisphere. Hence, the mass flow rate in the no magnetic field case is 1.5 times greater than in the simulation with magnetic field.

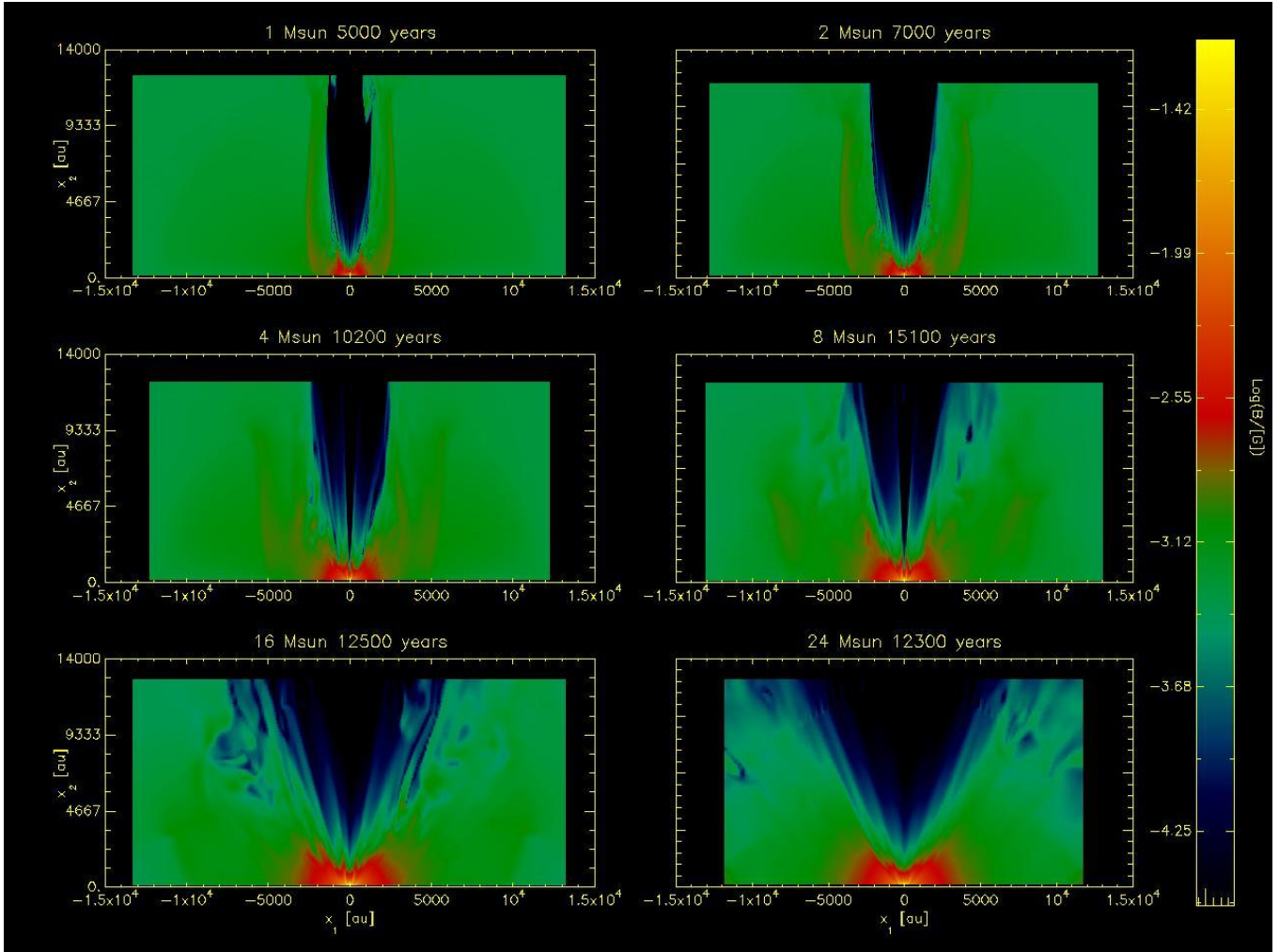


**Figure 6.** Slices through the middle of the grid showing the logarithm of the magnetic field strength at the end of each simulation.

### 3.5. Dependence on numerical resolution

As described in §2, we used a grid with  $140 \times 260 \times 260$  cells in our standard setup for these simulations (with  $m_* \geq 4 M_\odot$ ). To test the effect of grid resolution on the results, we also ran the  $4 M_\odot$  simulation using a grid with  $210 \times 380 \times 380$  cells (medium resolution), and using a grid with  $280 \times 520 \times 520$  cells (high resolution). Figure 15 compares the results of these simulations after 10,200 years of simulation time, at which point the protostar would have accreted  $2 M_\odot$ . While some differences are apparent in the density structures, the width of the flow is found to be approximately the same in all three cases. In particular,  $\theta_{\text{outflow}}$  in the high resolution simulation was found to be  $18.2^\circ$ , in the medium resolution simulation it was  $16.5^\circ$ , and in the standard low resolution simulation it is  $14.9^\circ$ .

Since a higher resolution simulation resolves the region around the axis better, the injection velocity will be higher in the innermost cells around the axis. This ultimately leads to larger velocities of the flow in the central regions in the higher resolution simulations. In all resolution runs, the flow begins to break out of the core after approximately 1,000 years of simulation time. We find that the mass flow rate, relative to the injected flow rate, differs a lot between the different resolutions

at earlier times. After 6,500 years we find the largest difference, with the mass flow rate in the high resolution run being almost an order of magnitude larger than in the “normal” run. However, after 10,000 years the mass flow rates in the different resolution simulations appear to be converging towards  $\approx 5 \times 10^{-5} M_\odot \text{ yr}^{-1}$ . The momentum rate does not show the same differences, and after 6,500 years the momentum rate in the high resolution run is a factor 1.5 larger than in the “normal” run, which is the largest deviation between the simulations that we find. After 10,000 years the momentum rate in the high resolution simulation is  $\approx 10\%$  larger than in the low resolution simulation. We are therefore satisfied that the resolution does not significantly affect the results of our simulations. We caution that neither the mass flow rate nor the momentum rate is constant throughout the grid, so these values are subject to the exact slice and time at which they are calculated.

We recall that we use a logarithmic grid, and that we aim at resolving the injection radius  $r_{\text{inj}}$  with 10 cells (see §2). Since in the 1 and  $2 M_\odot$  simulations the injection region is the smallest, these simulations therefore have the smallest cells (in the  $x_2$  and  $x_3$  directions), which therefore necessitates the biggest stretching of the grid in order to extend the grid beyond  $R_c$ , when using the same number of cells. The cells around the axis near

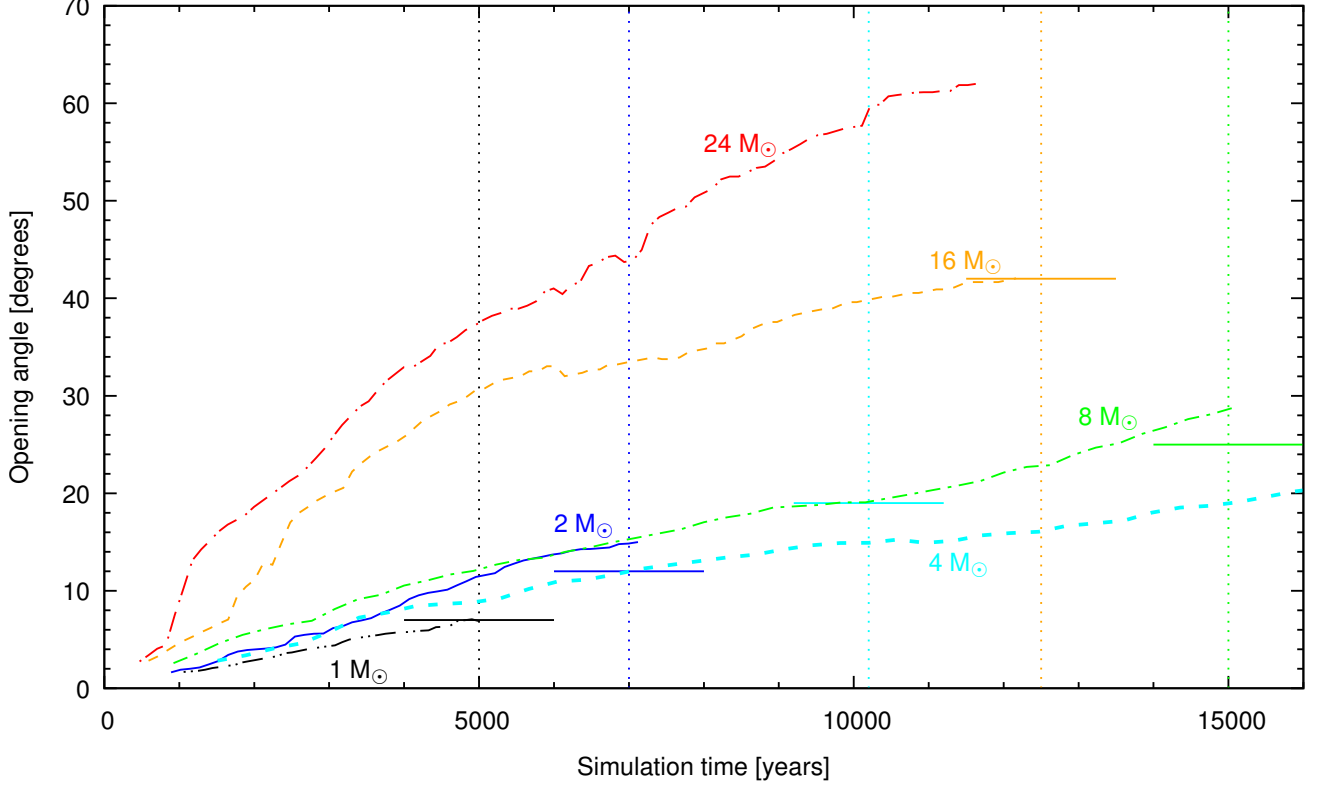


**Figure 7.** Opening angle of outflow cavity,  $\theta_{\text{outflow}}$ , as a function of simulation time for the runs with protostellar masses of  $1 M_{\odot}$  (black dot-dot-dash),  $2 M_{\odot}$  (solid blue line),  $4 M_{\odot}$  (cyan dashed line) and  $8 M_{\odot}$  (green long-dash short-dash line) and  $16 M_{\odot}$  (orange dashed line) and  $24 M_{\odot}$  (red long-dash dot line) for the case with no pre-cleared cavity. The colored vertical dotted lines show the times when the stars have accreted half the mass needed to take it to the next simulated model in the sequence. The horizontal line portions crossing the vertical lines indicate the opening angles found in the semi-analytic models of Zhang et al. (2014b).

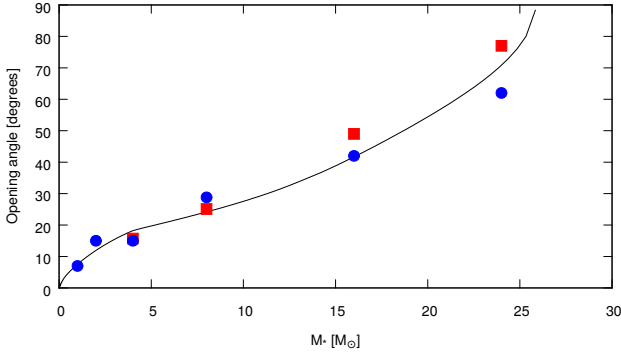


**Figure 8.** Outflow opening angle versus protostellar mass. Blue circles are the opening angles found in our fiducial simulations without pre-clearing. Red squares are the opening angles in the simulations with pre-clearing. The black line shows the results of the semi-analytic model of Zhang et al. (2014b).

the inner  $x_1$  boundary are cubic by design, so this also lead to small cells in the  $x_1$  direction near the injection boundary. In these  $1$  and  $2 M_{\odot}$  simulations, we found that when using the same resolution as the higher protostellar masses, the envelope develop a “noisy” density structure over time. This turned out to be related to the degree of stretching of the grid that we had to utilize to both resolve the injection radius with  $\sim 10$  cells, and resolve the whole envelope structure. Using more grid cells (in all directions, but in particular in the  $x_1$  direction), we found that we could reduce the noisiness of these sim-

ulations, however, the main results, i.e.,  $\theta_{\text{outflow}}$  and  $\dot{m}$ , were not affected.

#### 4. DISCUSSION AND SUMMARY

In our presented MHD simulations, we follow a sequence of evolutionary models of the protostar, enabled by injecting a disk wind into the simulation box at a height of  $100$  au above the disk. A number of other groups have performed collapse simulations to study outflows from massive protostars, using various numerical techniques and including different physics. However, most of these do not follow the evolution of the protostar until the end, and can therefore not estimate the star formation efficiency.

Some previous studies performed ideal-MHD simulations of  $100 M_{\odot}$  core collapse (Seifried et al. 2011, 2012; Hennebelle et al. 2011; Commerçon et al. 2011). Those MHD simulations showed especially that the fragmentation is suppressed by the magnetic breaking in the highly magnetized cases. However, they could not continue the simulation long enough to reach a  $\sim 5 M_{\odot}$  protostellar mass due to the high numerical cost of following the small-scale processes, i.e., the disk formation and the outflow launching.

The collapse of a massive cloud core was also simulated by Matsushita et al. (2017, 2018), who followed the protostar until it reached a mass of  $\sim 30 M_{\odot}$ , starting from a range of cloud masses. They found a similar mass ejection rate ( $\sim 10^{-4} M_{\odot} \text{ yr}^{-1}$ ) to what we found in their simulation with a cloud mass of  $77 M_{\odot}$ . However, their

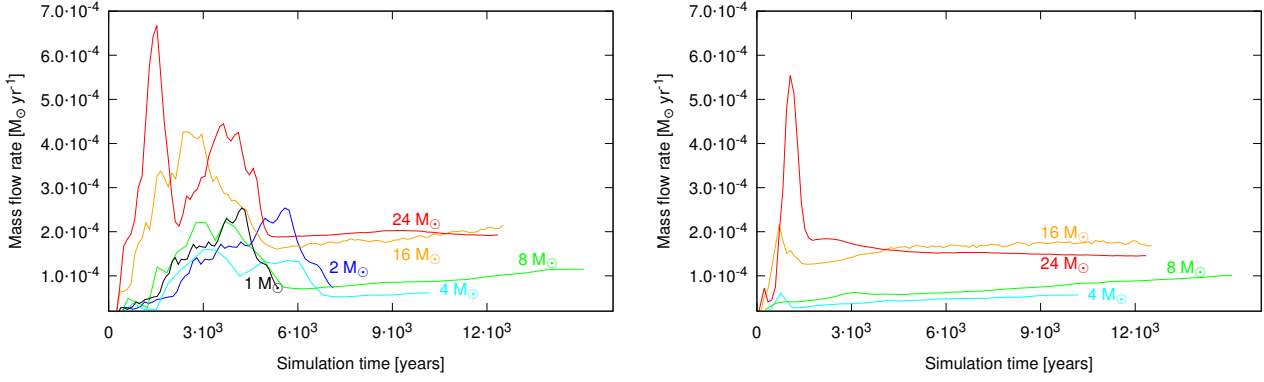


**Figure 9.** The mass flow rate (in one hemisphere) as a function of time for the simulations without pre-clearing (left panel), and with pre-clearing (right panel).

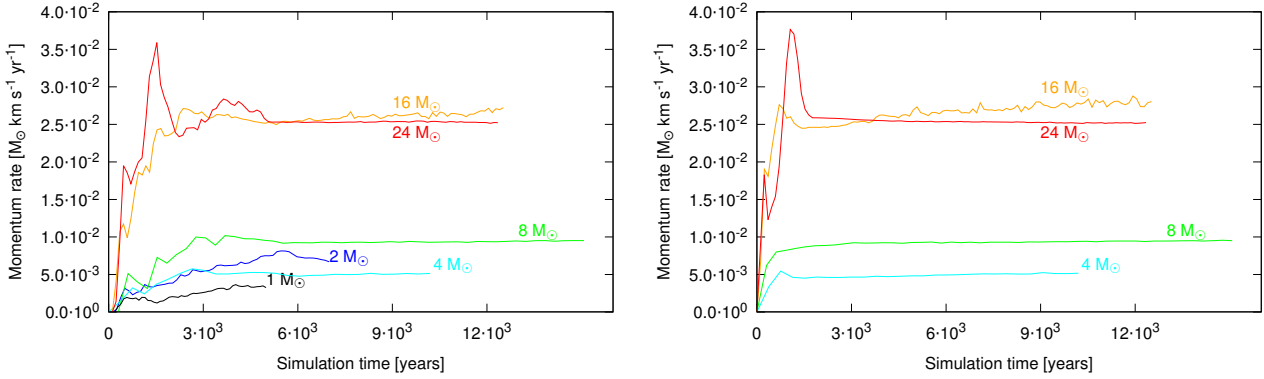


**Figure 10.** The momentum rate (in one hemisphere) as a function of time for the simulations without pre-clearing (left panel), and with pre-clearing (right panel).

momentum flux in their simulation with a core mass of  $385 M_{\odot}$  is similar to ours ( $\sim 10^{-2} M_{\odot} \text{ km s}^{-1} \text{ yr}^{-1}$ ).

However, since these works terminate the calculations before the star reaches its final mass, they can not estimate the star formation efficiency. This is one of the main objectives of this paper. We therefore simulated a sequence of models using boundary conditions relevant to the Turbulent Core Model that can be compared to the semi-analytic work of Zhang et al. (2014b).

Building on the model of Matzner & McKee (2000), Zhang et al. (2014b) evaluated the evolution of the outflow opening angle during the growth of a massive protostar. For their fiducial values, they found that a core with initial mass of  $60 M_{\odot}$  reaches a stage with an  $8 M_{\odot}$  protostar with an outflow with opening angle of  $25^{\circ}$ . Later it grows to a  $16 M_{\odot}$  protostar having an outflow with an opening angle of  $40^{\circ}$ . The final star resulting from their model had a mass of  $26 M_{\odot}$ . This is in reasonably good agreement with what we find in our study.

We have found that the opening angle increases with more massive protostars, i.e., with age, in agreement with the evolutionary sequence proposed in Beuther & Shepherd (2005). This is also in agreement with observations. Arce et al. (2007) found that outflows from early B and late O stars could have a collimation factor (i.e., length/width) greater than 5 for ages less than  $10^4$  yrs, although other sources have less well collimated flows also at early stages.

Since we find similar results to those in Zhang et al. (2014b) for outflow opening angles, we therefore also ob-

tain a SFE of  $\sim 50\%$ , similar to what they found. This is then an indication that such MHD disk winds may be a dominant mechanism for limiting the growth of the protostar and ultimately helping to shape the stellar initial mass function from a given pre-stellar core mass function.

Radiative feedback is also expected to have a significant impact on the formation of massive stars (Krumholz et al. 2009; Kuiper et al. 2010; Klassen et al. 2016; Rosen et al. 2016). However, the magnetically-driven outflow creates the cavity before the luminosity becomes sufficiently high to interfere with the mass accretion. Since the outflow cavity channels the radiation, the impact of radiative feedback is reduced (Yorke & Bodenheimer 1999; Krumholz et al. 2005; Kuiper et al. 2015). Recent studies including multiple feedback processes together show, at least in the case of cloud cores with  $M_c < 100 M_{\odot}$ , that the MHD disk wind is likely to be the dominant feedback mechanism determining the SFE (Tanaka et al. 2017; Kuiper & Hosokawa 2018). Based on these results, we conclude that the radiative processes would not alter our results.

We note that a limitation of applying our work to link CMF and IMF is that we have focused on single stars, but most massive stars are in binaries (Sana et al. 2012). Kuruwita et al. (2017) simulated outflows from the formation of both single and binary stars. While their simulations could not predict the final masses of the stars due to computational limitations, they found that the single star case accreted less mass compared to the binaries in the same amount of time. Hence single stars may have

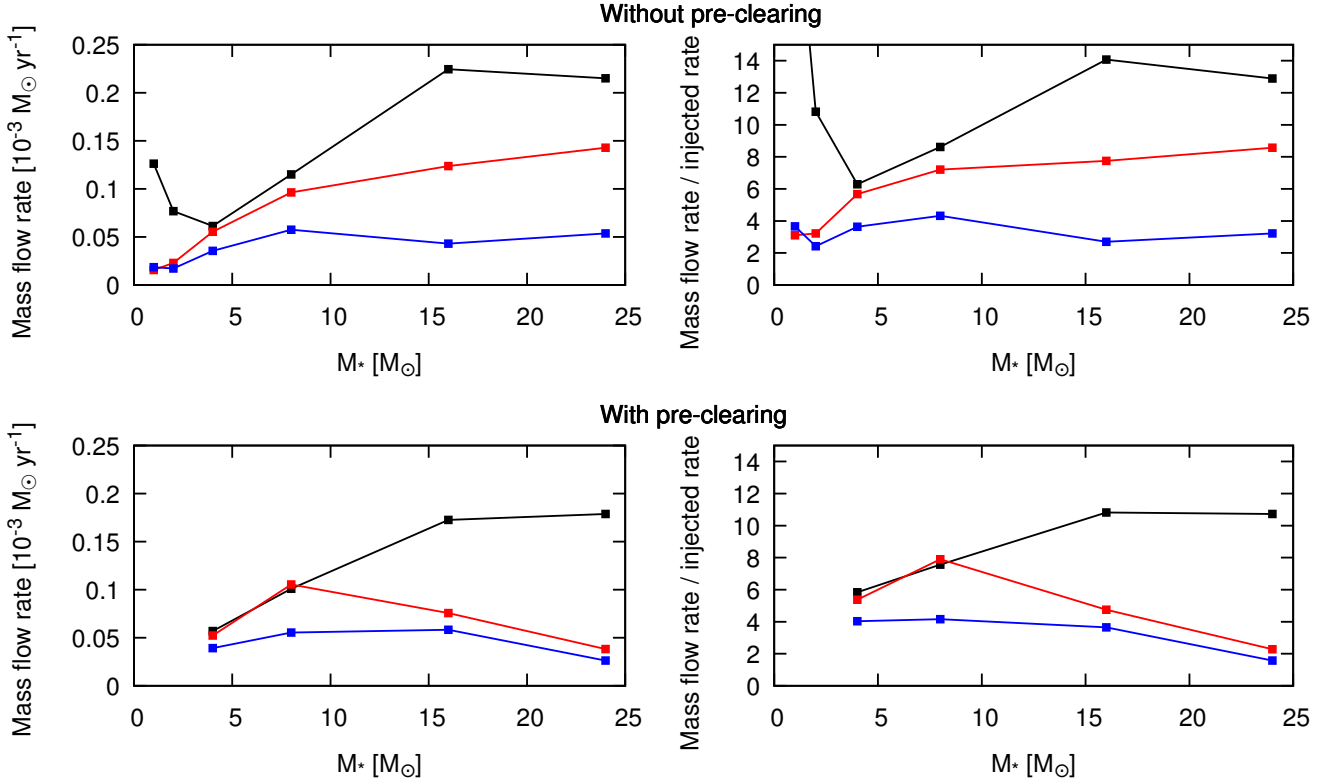


**Figure 11.** Mass outflow rate (in one hemisphere) at a height above the disk of  $1/10 R_c$  (blue curve),  $1/2 R_c$  (red curve), and  $R_c$  (black curve) as a function of the protostellar mass (left panels). The right panels show the same, but normalized to the injected flow rate (into one hemisphere). The top row is for the simulations without a pre-cleared cavity, the bottom row shows the simulations with a pre-cleared cavity.

a lower star formation efficiency than binary stars. Such an effect may be due to the relatively weaker outflows from two lower mass protostars compared to that of a single protostar with twice the mass.

We have compared the distributions of outflowing masses in our simulations with some observed cases, i.e., those found in C1-Sa and C1-Sb (Figure 4). In the blueshifted outflow, they found the majority of the outflowing material at velocities well below  $10 \text{ km s}^{-1}$ , while in the redshifted outflow it is more evenly distributed to  $\sim 30 \text{ km s}^{-1}$ , especially in C1-Sa. In our simulation, these distributions vary depending on the protostellar mass. In the  $1 M_{\odot}$  simulation, there is a peak around  $10 \text{ km s}^{-1}$ , while the  $8 M_{\odot}$  simulation shows a peak around  $3 \text{ km s}^{-1}$ , and the other simulations have a peak close to  $1 \text{ km s}^{-1}$ . The observed distributions of outflowing mass have a higher normalization and appear to drop off with a steeper power law at high velocities than in our simulations. We found that generally the power law is steeper in the lower protostellar mass simulations than in the higher.

Maud et al. (2015) found outflow momentum rates of  $10^{-3} - 10^{-1} M_{\odot} \text{ km s}^{-1} \text{ yr}^{-1}$  for outflows from core masses of  $\sim 60 M_{\odot}$  (luminosity of  $\sim 10^3 - 10^5 L_{\odot}$ ), while Beuther et al. (2002) found momentum rates of  $\sim 10^{-3} - 10^{-1} M_{\odot} \text{ km s}^{-1} \text{ yr}^{-1}$  for such outflows. This is in reasonable agreement with our results, which reflect our choice of input boundary conditions. We found momentum rates (leaving the core) of  $5 \times 10^{-3} - 3 \times 10^{-2} M_{\odot} \text{ km s}^{-1} \text{ yr}^{-1}$ . These works also found mass flow rates of the order  $10^{-4} - 10^{-3} M_{\odot} \text{ yr}^{-1}$  for sources

with luminosity of  $\sim 10^3 - 10^5 L_{\odot}$ , which is also in good agreement with our mass flow rates found to be  $0.5 - 2.5 \times 10^{-4} M_{\odot} \text{ yr}^{-1}$ .

We found that the momentum rate in our simulations (Figure 13) roughly follows the same trend as the best fit to the observational data in Wu et al. (2004), however, our points from the higher mass protostellar simulations are within the uncertainty range from Wu et al. (2004), while the points from the lower mass simulations are a factor a few above. The data in Wu et al. (2004) has a large scatter of about two orders of magnitude on either side of the best fit line, and therefore even our points from the low protostellar simulations are in better agreement with the best fit from Wu et al. (2004) than what it appears from Figure 13. Compared with Wu et al. (2004), Maud et al. (2015) found a very similar best fit line to their data, but have somewhat smaller scatter of the data.

Other observational constraints can be made by comparing  $B$ -field strengths in our simulations with observed values. The magnetic field in the massive cores from which massive stars form was measured by Beuther et al. (2018). They found field strengths of  $\sim 0.6 - 3.7 \text{ mG}$  in



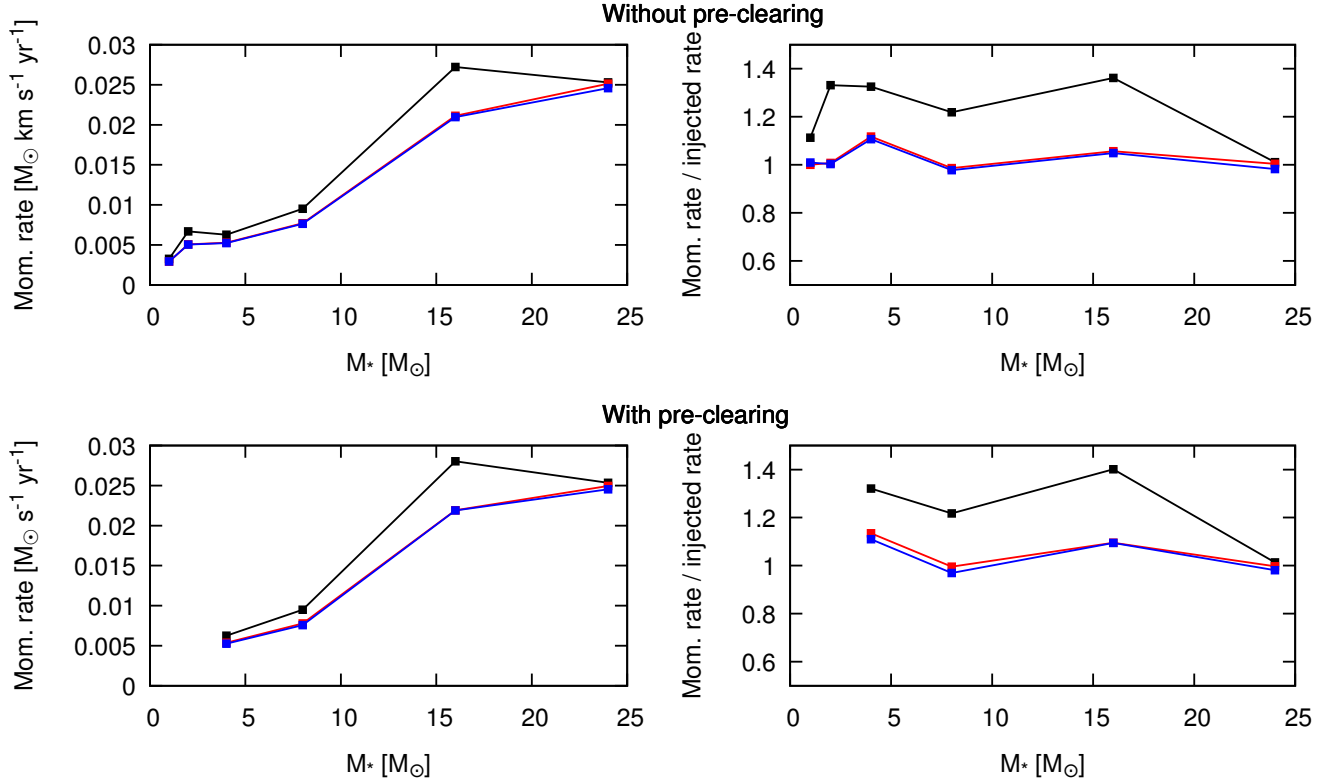


**Figure 12.** The outflowing momentum rate (in one hemisphere) at a height above the disk of  $1/10 R_c$  (blue curve),  $1/2 R_c$  (red curve), and  $R_c$  (black curve) as a function of the protostellar mass (left panels). The right panels show the same, but normalized to the injected rate (into one hemisphere). The top row is for the simulations without a pre-cleared cavity, the bottom row shows the simulations with a pre-cleared cavity.

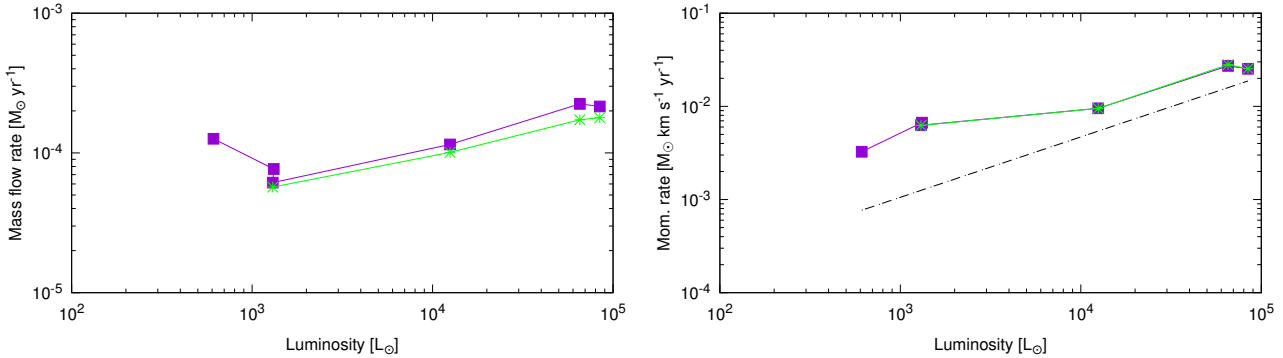


**Figure 13.** The mass flow rate (left panel) and momentum rate (right panel) in one hemisphere as a function of bolometric luminosity. The purple curve is for the simulations without pre-clearing, the green curve is for the simulations with pre-clearing. The dashed black line is the best fit from Wu et al. (2004).

the high-mass starless region IRDC 18310-4. Our initial setup, with a core scale mG magnetic field, is in reasonable agreement with these findings of the field strength in a high mass starless region by Beuther et al. (2018). Then for later stages, Vlemmings et al. (2010) found that in high density material in Cep A where the masers occur, the magnetic field strength is  $\sim 23$  mG. Surcis et al. (2009) and Dall’Olio et al. (2017) found that the small scale field probed by the masers are consistent with large scale fields traced by dust, and that the magnetic field structure is largely aligned with the jet-outflow direction (Beuther et al. 2010). Dall’Olio et al. (2017) also found that the field strength near the disk in the high mass pro-

tostar IRAS 18089 is  $\sim 12$  mG. Beuther et al. (2010); Vlemmings (2008) found magnetic field strengths of 11 and  $8 \mu\text{G}$  in high density regions of this source. We find magnetic field strengths at the base of the outflow approaching 100 mG, in agreement with the findings from Cep A and the high density and near disk region of IRAS 18089.

In summary, we have performed 3 dimensional magneto-hydrodynamic simulations of outflows from protostars of a sequence of protostellar models formed from a  $60 M_\odot$  core. We have found that the outflow generally becomes stronger and wider as the central object gets more massive, i.e., later in the evolution. Mass

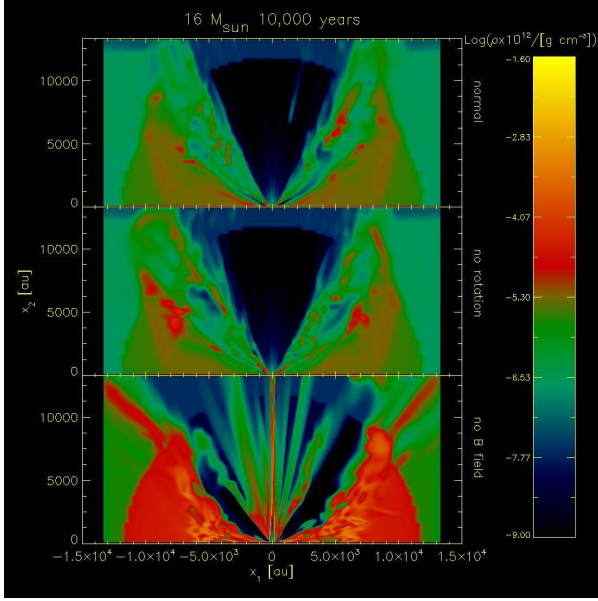


**Figure 14.** The  $16 M_{\odot}$  simulation after  $10^4$  years. The top panel shows the normal simulation, the middle panel shows the same setup except that the injected material is not given a rotational velocity. The bottom panel shows the same setup as the top panel, but with no magnetic field.

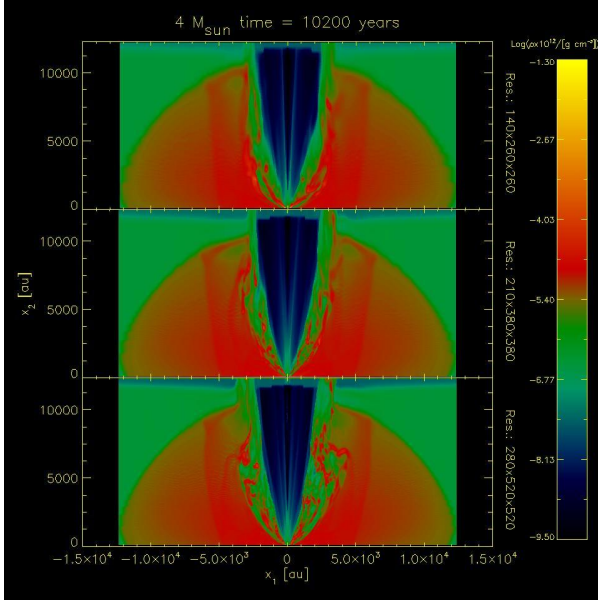


**Figure 15.** Comparison of the density structure through the middle of the grid of the  $4 M_{\odot}$  simulation in normal resolution (top panel), medium resolution (middle panel), and high resolution (bottom panel) after 10,200 years of simulation time.

flow rates, momentum rates, and outflow masses in our simulations are in reasonable qualitative agreement with observations. With these simulations, and this particular mass configuration, we find a star formation rate of  $\sim 50\%$ , in reasonably good agreement with the  $\sim 43\%$  found by the analytic calculations performed in Zhang et al. (2014b).

Part of this work was performed when J. E. S. was a post doc at the University of Florida. This work has been supported in part by NASA grant NNX15AP95A,

in part by NASA through grant HST-AR-15053 from the Space Telescope Science Institute, which is operated by AURA, Inc., under NASA contract NAS 5-26555, and in part by the University of Florida astro theory post doctoral fellowship program. This work was supported in part by NAOJ ALMA Scientific Research Grant number 2017-05A. We would like to thank Y. Zhang for helpful comments.

## REFERENCES

- Anderson, J. M., Li, Z.-Y., Krasnopolsky, R., & Blandford, R. D. 2006, *ApJ*, 653, L33
- André, P., Men'shchikov, A., Bontemps, S., et al. 2010, *A&A*, 518, L102
- Arce, H. G., Shepherd, D., Gueth, F., et al. 2007, *Protostars and Planets V*, 245
- Bacciotti, F., Mundt, R., Ray, T. P., et al. 2000, *ApJ*, 537, L49
- Beltrán, M. T., & de Wit, W. J. 2016, *A&A Rev.*, 24, 6
- Beuther, H., Schilke, P., Sridharan, T. K., et al. 2002, *A&A*, 383, 892
- Beuther, H., & Shepherd, D. 2005, in *Astrophysics and Space Science Library*, Vol. 324, *Astrophysics and Space Science Library*, ed. M. S. N. Kumar, M. Tafalla, & P. Caselli, 105
- Beuther, H., Vlemmings, W. H. T., Rao, R., & van der Tak, F. F. S. 2010, *ApJ*, 724, L113
- Beuther, H., Soler, J. D., Vlemmings, W., et al. 2018, *A&A*, 614, A64
- Blandford, R. D., & Payne, D. G. 1982, *MNRAS*, 199, 883
- Bonnell, I. A., Bate, M. R., Clarke, C. J., & Pringle, J. E. 2001, *MNRAS*, 323, 785
- Bonnell, I. A., Bate, M. R., & Zinnecker, H. 1998, *MNRAS*, 298, 93
- Caratti o Garatti, A., Stecklum, B., Linz, H., Garcia Lopez, R., & Sanna, A. 2015, *A&A*, 573, A82
- Carrasco-González, C., Rodríguez, L. F., Anglada, G., et al. 2010, *Science*, 330, 1209
- Cheng, Y., Tan, J. C., Liu, M., et al. 2018, *ApJ*, 853, 160
- Coffey, D., Bacciotti, F., & Podio, L. 2008, *ApJ*, 689, 1112
- Commerçon, B., Hennebelle, P., & Henning, T. 2011, *ApJ*, 742, L9
- Dall'Olivo, D., Vlemmings, W. H. T., Surcis, G., et al. 2017, *A&A*, 607, A111
- Hennebelle, P., Commerçon, B., Joos, M., et al. 2011, *A&A*, 528, A72
- Hirota, T., Machida, M. N., Matsushita, Y., et al. 2017, *Nature Astronomy*, 1, 0146
- Jørgensen, M. A. S. G., Ouyed, R., & Christensen, M. 2001, *A&A*, 379, 1170
- Klassen, M., Pudritz, R. E., Kuiper, R., Peters, T., & Banerjee, R. 2016, *ApJ*, 823, 28
- Königl, A., & Pudritz, R. E. 2000, *Protostars and Planets IV*, 759
- Könyves, V., André, P., Men'shchikov, A., et al. 2010, *A&A*, 518, L106
- Krumholz, M. R., Klein, R. I., McKee, C. o. F., Offner, S. S. R., & Cunningham, A. J. 2009, *Science*, 323, 754
- Krumholz, M. R., McKee, C. F., & Klein, R. I. 2005, *ApJ*, 618, L33
- Kuiper, R., & Hosokawa, T. 2018, *ArXiv e-prints*, arXiv:1804.10211
- Kuiper, R., Klahr, H., Beuther, H., & Henning, T. 2010, *ApJ*, 722, 1556
- Kuiper, R., Turner, N. J., & Yorke, H. W. 2016, *ApJ*, 832, 40
- Kuiper, R., Yorke, H. W., & Turner, N. J. 2015, *ApJ*, 800, 86
- Kuruwita, R. L., Federrath, C., & Ireland, M. 2017, *MNRAS*, 470, 1626
- Liu, M., Tan, J. C., Cheng, Y., & Kong, S. 2018, *ApJ*, 862, 105
- Lovelace, R. V. E., Berk, H. L., & Contopoulos, J. 1991, *ApJ*, 379, 696
- Lynden-Bell, D. 1996, *MNRAS*, 279, 389
- Machida, M. N., & Matsumoto, T. 2012, *MNRAS*, 421, 588
- Marti, J., Rodríguez, L. F., & Reipurth, B. 1993, *ApJ*, 416, 208
- Matsushita, Y., Machida, M. N., Sakurai, Y., & Hosokawa, T. 2017, *MNRAS*, 470, 1026

- Matsushita, Y., Sakurai, Y., Hosokawa, T., & Machida, M. N. 2018, *MNRAS*, 475, 391
- Matt, S., & Pudritz, R. E. 2005, *ApJ*, 632, L135
- Matzner, C. D., & McKee, C. F. 2000, *ApJ*, 545, 364
- Maud, L. T., Moore, T. J. T., Lumsden, S. L., et al. 2015, *MNRAS*, 453, 645
- McKee, C. F., & Tan, J. C. 2002, *Nature*, 416, 59
- . 2003, *ApJ*, 585, 850
- McLaughlin, D. E., & Pudritz, R. E. 1997, *ApJ*, 476, 750
- McLeod, A. F., Reiter, M., Kuiper, R., Klaassen, P. D., & Evans, C. J. 2018, *ArXiv e-prints*, arXiv:1801.08147
- Moll, R. 2009, *A&A*, 507, 1203
- Motte, F., Nony, T., Louvet, F., et al. 2018, *Nature Astronomy*, 2, 478
- Norman, M. L. 2000, in *Revista Mexicana de Astronomia y Astrofisica Conference Series*, Vol. 9, *Revista Mexicana de Astronomia y Astrofisica Conference Series*, ed. S. J. Arthur, N. S. Brickhouse, & J. Franco, 66–71
- Ouyed, R., Clarke, D. A., & Pudritz, R. E. 2003, *ApJ*, 582, 292
- Ouyed, R., & Pudritz, R. E. 1997, *ApJ*, 482, 712
- Ouyed, R., Pudritz, R. E., & Stone, J. M. 1997, *Nature*, 385, 409
- Ramsey, J. P., & Clarke, D. A. 2011, *ApJ*, 728, L11
- Ray, T., Dougados, C., Bacciotti, F., Eislöffel, J., & Chrysostomou, A. 2007, *Protostars and Planets V*, 231
- Romanova, M. M., Ustyugova, G. V., Koldoba, A. V., Chechetkin, V. M., & Lovelace, R. V. E. 1997, *ApJ*, 482, 708
- Rosen, A. L., Krumholz, M. R., McKee, C. e. F., & Klein, R. I. 2016, *MNRAS*, 463, 2553
- Sana, H., de Mink, S. E., de Koter, A., et al. 2012, *Science*, 337, 444
- Sanna, A., Surcis, G., Moscadelli, L., et al. 2015, *A&A*, 583, L3
- Seifried, D., Banerjee, R., Klessen, R. S., Duffin, D., & Pudritz, R. E. 2011, *MNRAS*, 417, 1054
- Seifried, D., Pudritz, R. E., Banerjee, R., Duffin, D., & Klessen, R. S. 2012, *MNRAS*, 422, 347
- Shibata, K., & Uchida, Y. 1985, *PASJ*, 37, 31
- Shu, F. H. 1977, *ApJ*, 214, 488
- Shu, F. H., Najita, J. R., Shang, H., & Li, Z.-Y. 2000, *Protostars and Planets IV*, 789
- Staff, J. E., Koning, N., Ouyed, R., Thompson, A., & Pudritz, R. E. 2015, *MNRAS*, 446, 3975
- Staff, J. E., Niebergal, B. P., Ouyed, R., Pudritz, R. E., & Cai, K. 2010, *ApJ*, 722, 1325
- Stute, M., Gracia, J., Vlahakis, N., et al. 2014, *MNRAS*, 439, 3641
- Surcis, G., Vlemmings, W. H. T., Dodson, R., & van Langevelde, H. J. 2009, *A&A*, 506, 757
- Tan, J. C., Beltrán, M. T., Caselli, P., et al. 2014, in *Protostars and Planets VI*, ed. H. Beuther, R. S. Klessen, C. P. Dullemond, & T. Henning, 149
- Tan, J. C., Kong, S., Zhang, Y., et al. 2016, *ApJ*, 821, L3
- Tanaka, K. E. I., Tan, J. C., & Zhang, Y. 2017, *ApJ*, 835, 32
- Uchida, Y., & Shibata, K. 1985, *PASJ*, 37, 515
- Vlemmings, W. H. T. 2008, *A&A*, 484, 773
- Vlemmings, W. H. T., Surcis, G., Torstensson, K. J. E., & van Langevelde, H. J. 2010, *MNRAS*, 404, 134
- Wu, Y., Wei, Y., Zhao, M., et al. 2004, *A&A*, 426, 503
- Yorke, H. W., & Bodenheimer, P. 1999, *ApJ*, 525, 330
- Zhang, Q., Qiu, K., Girart, J. M., et al. 2014a, *ApJ*, 792, 116
- Zhang, Y., & Tan, J. C. 2018, *ApJ*, 853, 18
- Zhang, Y., Tan, J. C., & Hosokawa, T. 2014b, *ApJ*, 788, 166
- Zhang, Y., Tan, J. C., & McKee, C. F. 2013a, *ApJ*, 766, 86
- Zhang, Y., Tan, J. C., De Buizer, J. M., et al. 2013b, *ApJ*, 767, 58
- Zhang, Y., Arce, H. G., Mardones, D., et al. 2016, *ApJ*, 832, 158